Anomalous Li Storage Capability in Atomically Thin Two-Dimensional Sheets of Nonlayered MoO2

Chuan Xia,[†] Yungang Zhou,[‡] Dhinesh Babu Velusamy,[†] Abdiaziz A. Farah,[§] Peng Li,[†] Qiu Jiang,[†] Ihab N. Odeh,[‖] Zhiguo Wang,[‡] Xixiang Zhang,[†] and Husam N. Alshareef*,[†]

[†]Materials Science and Engineering, King Abdullah University of Science and Technology (KAUST), Thuwal 23955-6900, Saudi Arabia

[‡]School of Physical Electronics, University of Electronic Science and Technology of China, Chengdu 610054, People's Republic of China

[§]Corporate Research and Innovation Center, Saudi Basic Industries Corporation (SABIC), Thuwal 23955-6900, Saudi Arabia

[‖]Saudi Basic Industries Corporation (SABIC), Sugar Land, Texas 77478, United States

S *Supporting Information*

ABSTRACT: Since the first exfoliation and identification of graphene in 2004, research on layered ultrathin two-dimensional (2D) nanomaterials has achieved remarkable progress. Realizing the special importance of 2D geometry, we demonstrate that the controlled synthesis of nonlayered nanomaterials in 2D geometry can yield some unique properties that otherwise cannot be achieved in these nonlayered systems. Herein, we report a systematic study involving theoretical and experimental approaches to evaluate the Li-ion storage capability in 2D atomic sheets of nonlayered molybdenum dioxide (MoO_2). We develop a novel monomer-assisted reduction process to produce high quality 2D sheets of nonlayered MoO_2. When used as lithium-ion battery (LIB) anodes, these ultrathin 2D-MoO_2 electrodes demonstrate extraordinary reversible capacity, as high as 1516 mAh g^{-1} after 100 cycles at the current rate of 100 mA g^{-1} and 489 mAh g^{-1} after 1050 cycles at 1000 mA g^{-1}. It is evident that these ultrathin 2D sheets did not follow the normal intercalation-cum-conversion mechanism when used as LIB anodes, which was observed for their bulk analogue. Our ex situ XPS and XRD studies reveal a Li-storage mechanism in these 2D-MoO_2 sheets consisting of an intercalation reaction and the formation of metallic Li phase. In addition, the 2D-MoO_2 based microsupercapacitors exhibit high areal capacitance (63.1 mF cm^{-2} at 0.1 mA cm^{-2}), good rate performance (81% retention from 0.1 to 2 mA cm^{-2}), and superior cycle stability (86% retention after 10,000 cycles). We believe that our work identifies a new pathway to make 2D nanostructures from nonlayered compounds, which results in an extremely enhanced energy storage capability.

KEYWORDS: Two-dimensional, nonlayered, MoO_2, Li-storage, microsupercapacitor
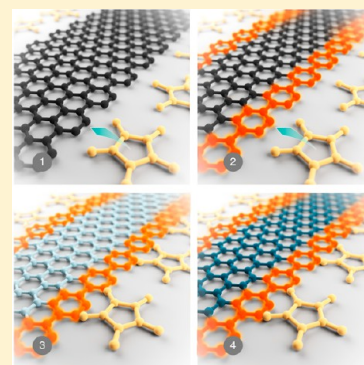
Realization of high-efficiency electrochemical energy storage solutions is one of the greatest challenges obstructing a truly sustainable future. To tackle this issue, researchers worldwide have been intensely developing lithium-ion batteries (LIBs) and supercapacitors with ever-increasing energy and power densities.[1−3] Since their introduction in the early 1990s, LIBs have predominantly been used as power sources for portable electronics.[4] Increasingly, however, LIBs are being developed to help realize the goal of electric vehicles and grid-scale energy storage.[5] Progress in the understanding and synthesis of insertion materials spurred the rise of currently commercialized LIBs. However, the limited energy/power density and cycle life of the commercial Li-ion intercalation cells, which is close to its technological limit, has increased the importance of developing new and disruptive technologies.[6] Capacitive energy storage using supercapacitors is characterized by very short charging times, which establishes them as high power density devices.[7] This high power capability is a direct result of the fact that the electrochemical process only occurs at or near the surface of capacitive electrode materials. Unfortunately, this high power is accompanied by relatively low energy density, which has always been a drawback of supercapacitors. Hence, the search for advanced electrode materials that fulfill the twin goal of high energy and power densities has accelerated at an unprecedented rate. An energy storage device that can deliver both high reversible capacity and high rate capability in a cost-effective way would be the state of the art of energy storage devices.

Molybdenum dioxide (MoO_2) has demonstrated promise as an electrode material for lithium ion storage due to its metallic conductivity (8.8×10^{-5} Ω cm at 300 K) and high theoretical capacity (up to 840 mAh g^{-1}).[7−11] For example, Chen et al.
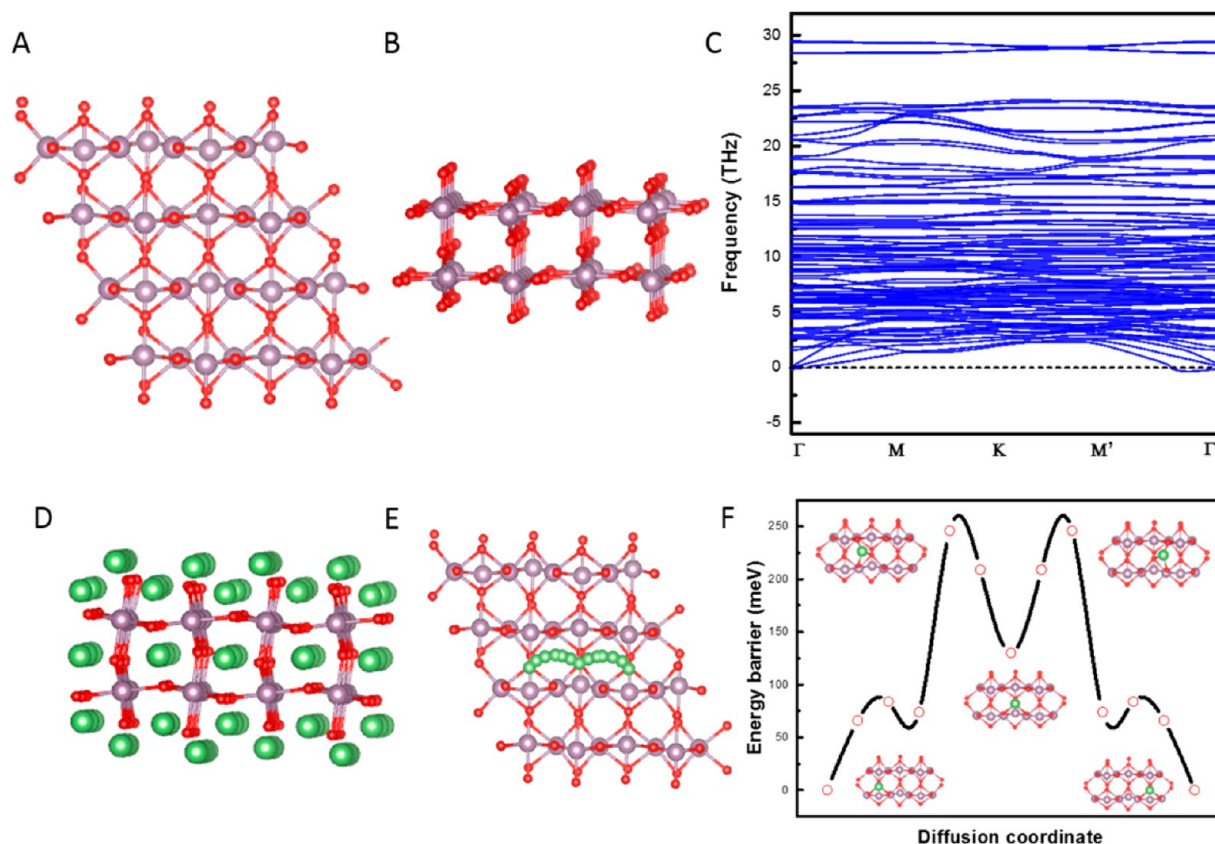
Figure 1. Theoretical predictions of 2D-MoO$_2$ for Li-ion storage. (A) Top view and (B) side view of the atomic arrangements in the structure of a monolayer 2D-MoO$_2$. (C) The DFT calculated phonon dispersion curves of monolayer 2D-MoO$_2$. (D) The stable Li-intercalated structure of monolayer 2D-MoO$_2$, which shows a theoretical capacity of 493 mAh g^{-1} for Li-ion storage. (E) The representative Li diffusion pathway along the 2D-MoO$_2$ surface and (F) its corresponding energy profile. Green, Li atom; purple, Mo atom; red, O atom.

have reported that ultrafine MoO$_2$ rods deliver a high reversible capacity of 830 mAh g^{-1} after 29 cycles at 0.05 C and 260 mAh g^{-1} at 1 C when used as LIB anodes.[11] Dunn et al. have demonstrated that nanosized-MoO$_2$/rGO electrodes could achieve a pseudocapacitance (Li capacity) of 150 mAh g^{-1} at a rate of 50 C.[7] The crystal structure of nonlayered MoO$_2$ is a distorted version of the rutile structure, which is constructed from a tunnel framework (Figure S1). In monoclinic MoO$_2$, Mo—Mo pairing along the Mo atom chains doubles the unit cell length in that direction and lowers the symmetry from tetragonal (rutile) to monoclinic MoO$_2$.[12] The presence of intracrystal tunnels in MoO$_2$ makes it possible to reversibly insert/extract Li-ions. Generally, lithium-ion-based charge storage in MoO$_2$ occurs through two distinct mechanisms: (i) Li$^+$ ion insertion/deinsertion into the tunnel sites, which offers a reversible capacity of 210 mAh g^{-1} (1.0 to 3.0 V, vs Li/Li$^+$) and (ii) a three-electron electrochemical conversion reaction below 1.0 V (630 mAh g^{-1}).[12,13]

However, recent reports have noted that an abnormal lithium-storage capability can be achieved in nanosized MoO$_2$. Stucky et al. have reported that mesoporous MoO$_2$ exhibits a discharge capacity of 1814 mAh g^{-1} for the first cycle and almost maintains its initial capacity after 50 cycles (1594 mAh g^{-1}). They have revealed that the Li-storage mechanism in this nanosized MoO$_2$ electrode was not actually based on a conversion reaction (Li$_x$MoO$_2$ → Mo + Li$_2$O). Instead, they attributed the anomalously high capacity they observed to the formation of a metallic Li-rich phase around the Li-ion-intercalated MoO$_2$ phase (Li$_x$MoO$_2$).[6] While the preparation of

nanosized MoO$_2$ in the above-mentioned report involves complex processes (hard templating and subsequent HF etching) and high cost, these findings indicate that MoO$_2$ electrodes may be able to achieve both high-energy and high-power densities, but a simple route to processing ultrathin MoO$_2$ is needed.

Because of the first exfoliation and identification of graphene in 2004,[14] research on layered ultrathin two-dimensional (2D) nanomaterials has achieved remarkable progress. Ultrathin 2D nanomaterials are sheet-like structures with a thickness of a single or a few atomic layers (typically less than 5 nm) but with a lateral size larger than 100 nm and possibly up to tens of micrometers.[15] Owing to the ultrahigh surface-to-volume ratio, extremely short ion-diffusion path, and strong quantum confinement of electrons in two dimensions, these ultrathin 2D materials often display significantly improved energy storage and conversion properties compared to their bulk counterparts.[16−20]

Realizing the special importance of 2D geometry, methods for controlled synthesis of nonlayered nanomaterials in 2D geometry are urgently needed. Therefore, we predict that the Li-ion storage capability of MoO$_2$ could be significantly enhanced if we find a way to synthesize atomic-scale 2D sheets of nonlayered MoO$_2$. Although the solution synthesis of atomic-scale 2D sheets of MoO$_2$ has never been realized, in reality there are multiple scientific arguments that make this goal attractive: (1) The ultrathin nature of 2D MoO$_2$ will greatly shorten the diffusion length for Li ions, which can enable electrochemical reactions that typically cannot occur in
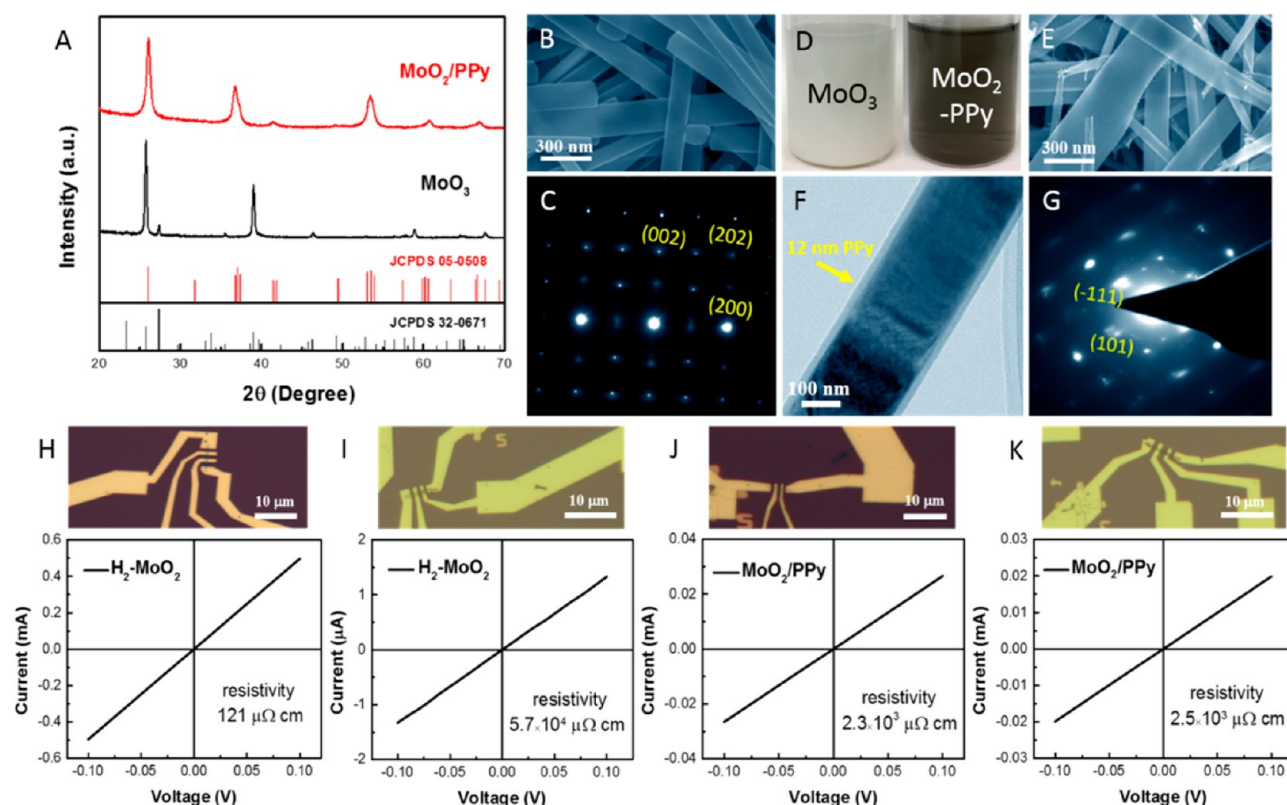
Figure 2. Characterization of MoO$_3$ nanoribbon and MoO$_2$/PPy core−shell structure. (A) XRD pattern of MoO$_3$ and MoO$_2$/PPy composites. (B) SEM image and (C) selected area electron diffraction (SAED) image of as-prepared MoO$_3$ nanoribbons. (D) Digital photo of MoO$_3$ nanoribbon dispersion before (white) and after (black) pyrrole reduction under hydrothermal conditions. (E) SEM and (F) TEM images of pyrrole-reduced MoO$_2$/PPy, as well as the corresponding (G) SAED image. The I−V curves of individual H$_2$−MoO$_2$ nanoribbon (H) before and (I) after one month of exposure to ambient air. The I−V profiles of individual MoO$_2$/PPy nanoribbon (J) before and (K) after one month of exposure to ambient air.

the bulk analogue.[6] (2) The ultrahigh surface area of 2D MoO$_2$ can open up the possibility to introduce extra Li intercalation sites. (3) A faster Li ions diffusion coefficient can be expected for these ultrathin 2D MoO$_2$ sheets.[21]

Herein, we report a systematic study involving theoretical and experimental approaches to evaluate the Li-ion storage capability in 2D atomic sheets of nonlayered MoO$_2$ (henceforth referred to as 2D-MoO$_2$). Solution-phase growth of single-unit-cell- and few-unit-cell-thick 2D MoO$_2$ sheets with a well-defined ribbon shape was achieved, and the details of the 2D-MoO$_2$ growth mechanism are elucidated. We demonstrate through theoretical and experimental approaches that 2D-MoO$_2$ exhibit excellent electrochemical performance that is suitable for LIB and microsupercapacitor applications.

Theoretical studies have frequently been employed to provide atomic-level insight into the structural stability and electrochemical properties of electrode materials.[22,23] Therefore, we first used density function theory (DFT) and ab initio molecular dynamics simulation (AIMD) to simulate the Li-ion storage in ultrathin 2D-MoO$_2$ to determine if ultrathin 2D-MoO$_2$ is indeed a promising Li-ion storage candidate. Figure 1A,B displays the atomic arrangements in the structure of the 2D-MoO$_2$ monolayer. Note that the 2D-MoO$_2$ layer still preserves its tunnel structure framework. Calculated cohesive energy of this structure is approximately 4.48 eV atom^{-1}. Compared to the values of 3.98 eV atom^{-1} in silicene, 3.26 eV atom^{-1} in germanene, and 3.46 eV atom^{-1} in Cu$_2$Si monolayer,[24] such a high cohesive energy implies that the

MoO$_2$ monolayer is a strongly bonded network. We then calculated its corresponding phonon dispersion curves to check the stability of the monolayer 2D-MoO$_2$. As Figure 1C conveys, besides the negligible imaginary frequencies near the Γ-point, all vibrational modes are real in the whole Brillouin zone. This result indicates that the 2D-MoO$_2$ monolayer will be kinetically stable if the wavelength of this particular mode is relatively smaller.[25,26] Furthermore, we noticed that the 2D-MoO$_2$ sheet retains its original structure after a 3000-step AIMD calculation (Figure S2), indicating that the monolayer 2D-MoO$_2$ is thermally stable. Interestingly, we found that the theoretical Li-ion intercalation capacity of monolayer 2D-MoO$_2$ is 493 mAh g^{-1} (Figure 1d and Figure S3), which is more than twice that of its bulk MoO$_2$ analogue (210 mAh g^{-1}). The calculated average Li adsorption energy is about −1.40 eV, reflecting a strong adsorption ability of 2D-MoO$_2$ for Li at high concentration. We also investigated the Li-ion diffusion barriers in 2D-MoO$_2$, which are crucial for the charging rate performance of Li-ion storage devices. The most possible diffusion pathway and the corresponding energy profiles are given, respectively, in Figure 1E,F. Of note, the calculated adsorption energy of Li atom in the tunnel site was 0.71 eV larger than that on the surface; thus, the Li atom is especially difficult to adsorb and diffuse along the tunnel directions. For the case of Li diffusion along the surface direction, we calculated a diffusion barrier of only 254 meV. The Li diffusion barrier value of the 2D-MoO$_2$ is lower or nearly the same as those of typical layered materials, such as monolayer graphene
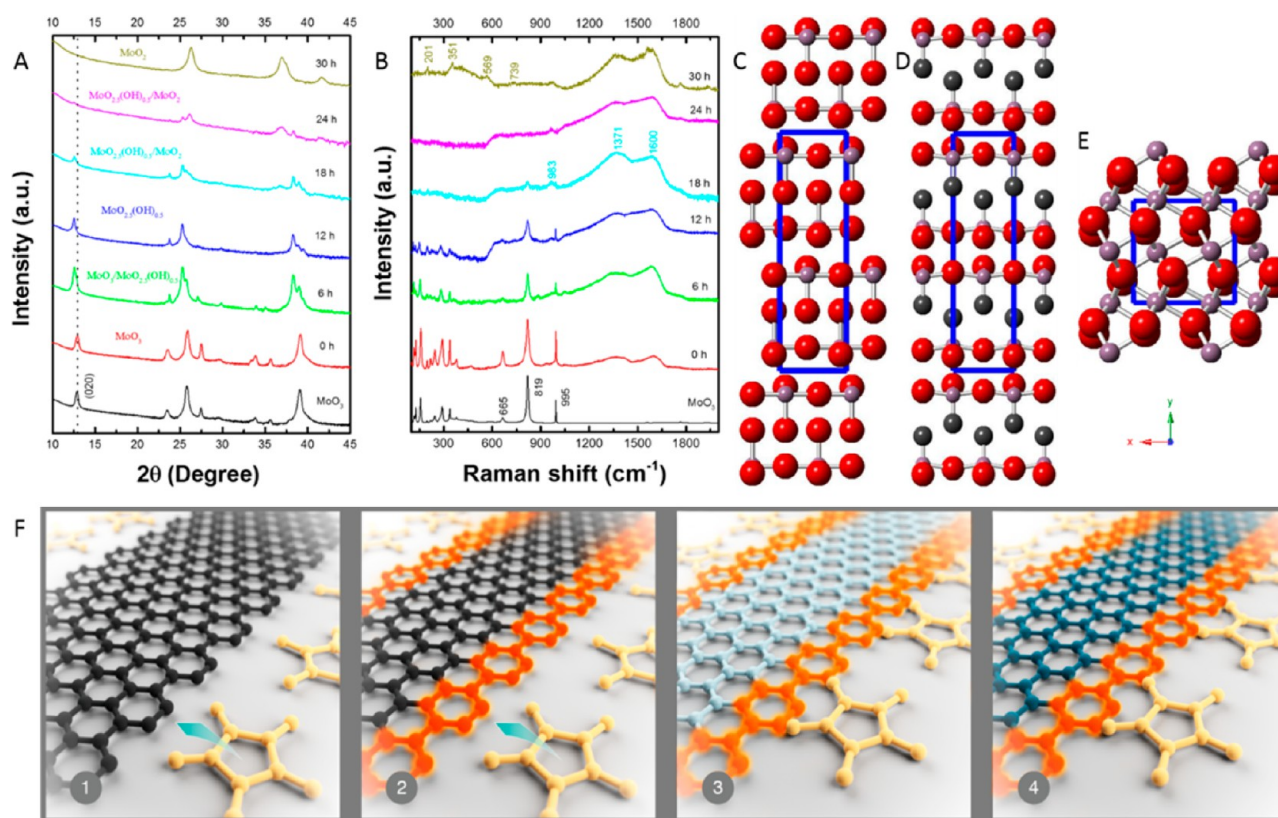
Figure 3. Tracking the phase evolution of MoO_3 nanoribbon during hydrothermal reaction. (A) Ex situ XRD pattern and (B) ex situ Raman spectra of hydrothermal products of homogeneous MoO_3-pyrrole solution at different stages (from 0 to 30 h). The crystal structure of (C) orthorhombic-layered MoO_3, (D) orthorhombic-layered $MoO_{2.5}(OH)_{0.5}$, and (E) monoclinic MoO_2. Note that the blue rectangles represent their unit cell. Red, O atom; purple, Mo atom; black, O atom and OH group. (F) Schematic illustration of the reaction pathway for the pyrrole-induced topotactical reduction ($MoO_3 \rightarrow MoO_{2.5}(OH)_{0.5} \rightarrow MoO_2$). The black, orange, light blue, and dark blue ribbons represent the MoO_3, PPy, $MoO_{2.5}(OH)_{0.5}$, and MoO_2, respectively. The atomic arrangements shown are not the actual crystal structure and are only intended for illustration purposes. The yellow, pentagonal, and small molecular represents the pyrrole monomer. In panel F, panels 1 and 2 represent the process of PPy formation on the MoO_3 nanoribbon during the preparation of MoO_3-pyrrole homogeneous aqueous solution; panels 2 and 3 illustrate the topotactic transformation of MoO_3; then panels 3 and 4 shows the formation of MoO_2 from the intermediate.

(327 meV),[27] MoS_2 (250 meV),[19] VS_2 (220 meV),[19] and silicene (230 meV),[28] which highlights its advantages as a Li storage electrode material. These findings suggest that the 2D-MoO_2 atomic sheets are indeed more favorable than bulk MoO_2 for Li-ion storage.

We have developed a monomer-assisted solution approach to synthesize highly conductive atomic scale sheets of 2D-MoO_2. In our synthesis strategy, a hydrothermal process first prepared the single-crystal MoO_3 nanoribbons precursor, which was then topotactically converted into 2D-MoO_2 with the assistance of the pyrrole monomer (see details in Methods). This yielded well-defined core−shell MoO_2-polypyrrole (MoO_2/PPy) nanoribbons. The X-ray diffraction (XRD) pattern, Raman, and X-ray photoelectron (XPS) spectra (Figure 2A and Figure S4a,b) confirm the high phase purity of the as-prepared bulk MoO_3. Scanning electron microscopy (SEM) and transmission electron microscopy (TEM) images (Figure 2B and Figure S5) show that MoO_3 nanoribbons with good morphology, purity, and homogeneity have been synthesized. The corresponding selected area electron diffraction (SAED) pattern of an individual MoO_3 nanoribbon (Figure 2C) confirms its single-crystalline nature. As Figure S4c illustrates, it is clear that these MoO_3 nanoribbons are about 70 nm thick. These nanoribbons were then reacted with pyrrole at 160 °C to produce MoO_2 (see Figure 2D; the digital photo of MoO_3

aqueous dispersion before and after pyrrole treatment). Interestingly, the white MoO_3 dispersion turns black after pyrrole treatment. The Raman spectra (Figure S4d) indicates that the newly formed black precipitates exhibit Raman peaks at 201, 351 569, and 739 cm^{-1} (which can be assigned to metallic MoO_2)[29] and at 983, 1370, and 1600 cm^{-1} (which can be assigned to PPy).[30] This result is additionally demonstrated by the XRD pattern shown in Figure 2a, where the MoO_2 diffraction pattern is clearly obtained. Moreover, the SEM and TEM images (Figure 2E,F) depict the well-defined core−shell structure of the resulting MoO_2/PPy nanoribbons. It is worth noting that the pyrrole-induced transformation to MoO_2 still retains the original nanoribbon morphology of MoO_3. It is also particularly interesting that our process results in MoO_2 with quasi-single-crystal nature (Figure 2G), which is beneficial for fast electron transportation. These findings clearly reveal that the high-valence state Mo^{6+} in MoO_3 was reduced to low-valence state Mo^{4+} during the hydrothermal reaction with pyrrole monomer, while simultaneously inducing in situ oxidative polymerization of monomer pyrrole to PPy. The next section discusses the growth mechanism of MoO_2/PPy core−shell nanoribbons.

Previous reports have indicated that nanostructured MoO_2 is susceptible to surface oxidation and that the resulting surface oxides can greatly impede the charge transfer reactions.[7,31]
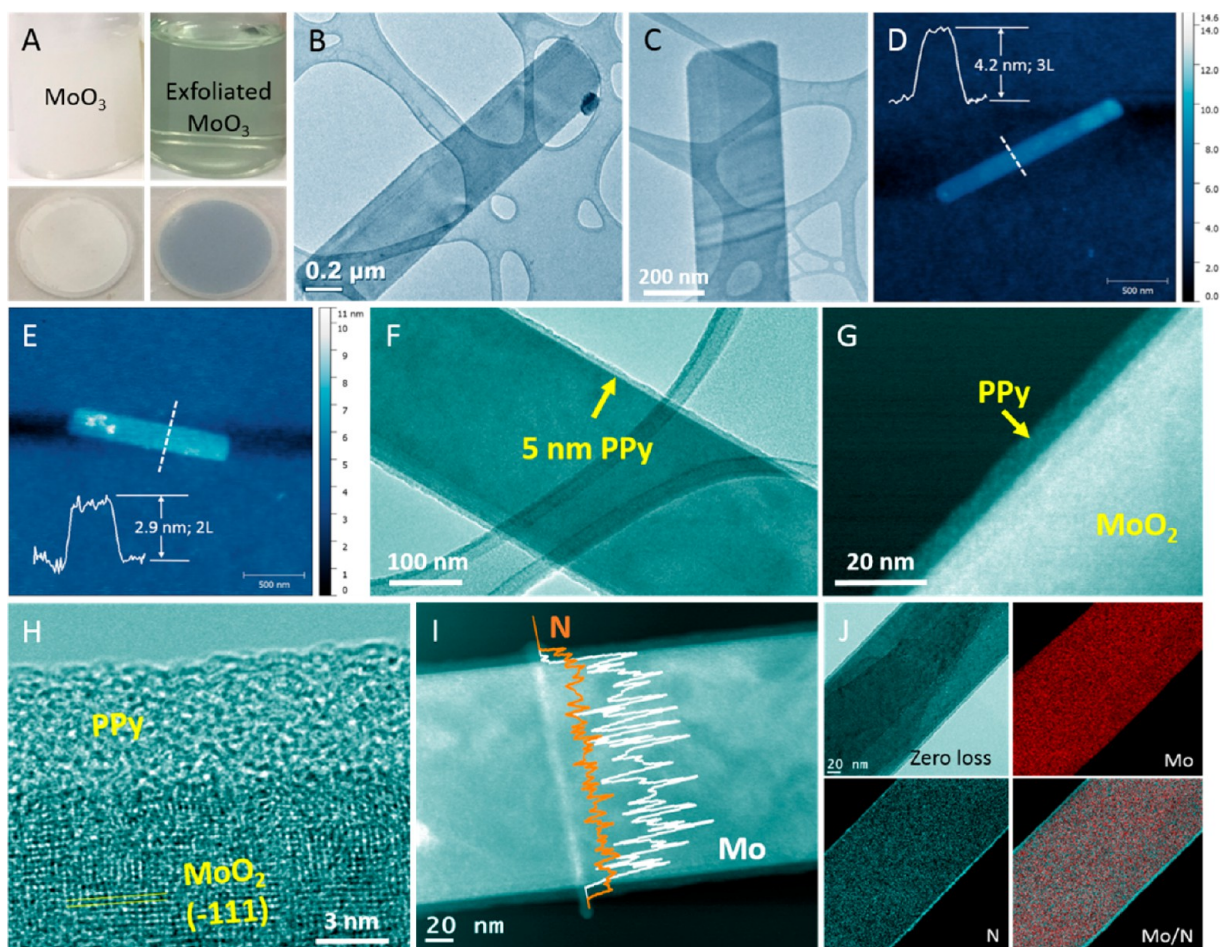
Figure 4. Characterization of delaminated MoO_3 nanoribbon and corresponding ultrathin 2D-MoO_2 sheets. (A) Digital photo of as-made and exfoliated MoO_3 nanoribbon dispersion and corresponding thin film. (B,C) TEM and (D,E) AFM images of exfoliated MoO_3 nanoribbon, displaying their ultrathin nature (only a few atomic layers). (F) TEM, (G) STEM, and (H) HRTEM images of ultrathin 2D MoO_2/PPy (2D-MoO_2). (I) Electron energy loss spectroscopy (EELS) line scan of individual MoO_2/PPy nanoribbon; the orange and white lines represent counts of nitrogen and molybdenum signals. (J) The energy-filtered transmission electron microscopy (EFTEM) elemental mapping of nitrogen and molybdenum.

However, in our process the surface in situ formed PPy layer protects the MoO_2 core from further oxidation. The XPS analysis of MoO_2/PPy (Figure S4e) confirms that Mo^{4+} is the dominant oxidation state at the surface, whereas those in previous literature reports on MoO_2 showed higher surface oxidation states (Mo^{5+} and Mo^{6+}).[7,32] To more directly demonstrate the role of PPy as a surface protective layer, we compared the electrical conductivities of the as-synthesized MoO_2 nanoribbon to those that had undergone one month of exposure in ambient air. We also compared our monomer-assisted produced MoO_2 nanoribbons (MoO_2/PPy) to those formed by the commonly practiced H_2-reduction method with similar nanoribbon morphology (H_2–MoO_2, see details in Methods). Figure 2H,I displays that the resistivity of the individual H_2–MoO_2 nanoribbon increased from 121 to 57000 $\mu\Omega$ cm after exposure to ambient air for one month, implying the formation of insulating MoO_x at the surface. In contrast, the MoO_2/PPy nanoribbons (Figure 2J,K) reflected a significantly smaller increase in resistance (2300–2500 $\mu\Omega$ cm) over the same period. This clearly demonstrates the stability of MoO_2/PPy core−shell nanoribbons against surface oxidation. These findings strongly suggest that the introduction of the pyrrole monomer during the hydrothermal process not only induces the topotactic transformation of MoO_3 to MoO_2, but also

protects the MoO_2 from surface oxidation. Because MoO_2/PPy can retain good conductivity, we expected that it could actually enhance Li-ion storage performance. Moreover, as Figure S4f indicates, our thermogravimetric analysis (TGA) revealed the weight ratio of MoO_2 and PPy in MoO_2/PPy composites to be 65% and 35%, respectively.

It should be noted that other reducing agents (such as ethanol[8,33,34] and H_2 gas[31,35]) can reportedly induce the conversion of MoO_3 nanoribbon to MoO_2, but they all require high temperature (≥ 600 °C) processing and/or involve post-treatments and nanoparticle products. These issues highlight the advantages of our pyrrole-monomer-assisted synthesis approach. More importantly, the present method is quite general and can be used to topotactically synthesize other low-valence-state metal oxides/sulfides (or even metals) with unique architecture. As an example, we show that uniform V_2O_3 nanorod arrays can be topotactically prepared from a V_2O_5 nanorod template using the same PPy approach (Figure S6). To understand the details of the phase transformation from MoO_3 nanoribbons to MoO_2, we carried out time-dependent ex situ XRD and Raman studies. Figure 3a depicts the ex situ XRD patterns of pristine MoO_3 and of the MoO_3-pyrrole homogeneous mixture (referred to as 0 h) and the corresponding hydrothermal products at different hydrothermal
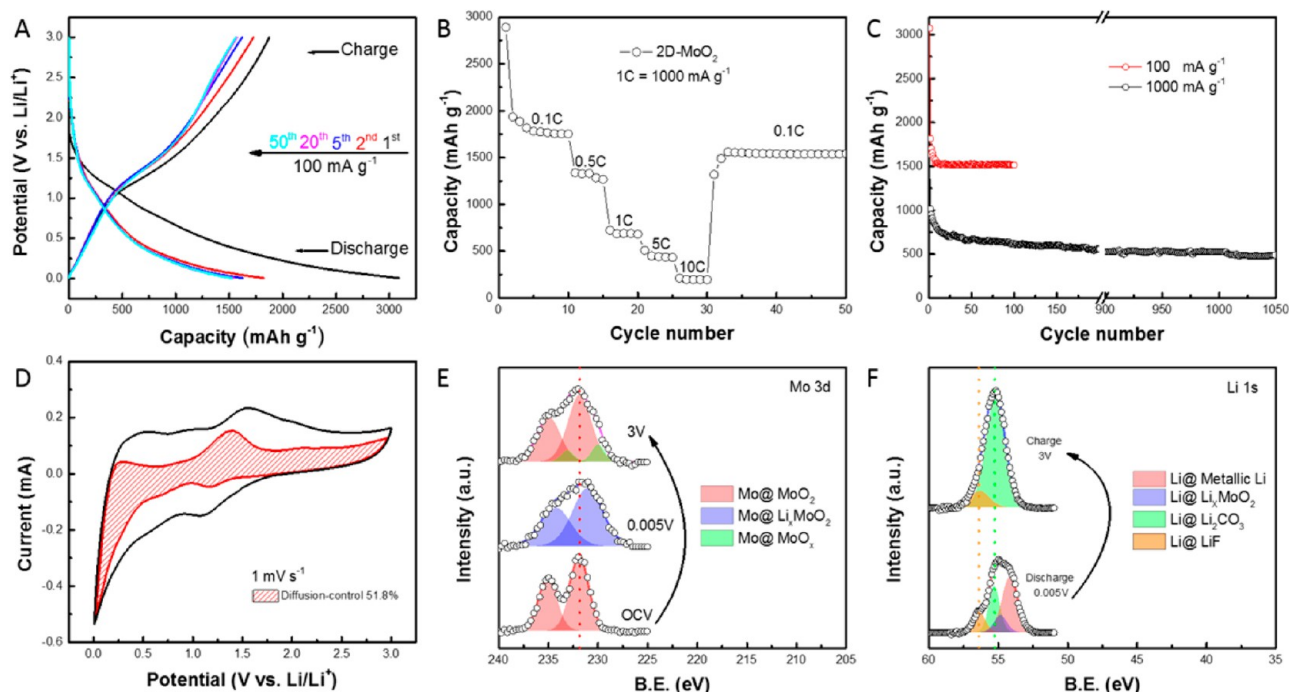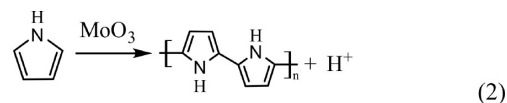
Figure 5. Electrochemical analysis of ultrathin 2D-MoO$_2$ sheets as LIB anodes. (A) Galvanostatic charge−discharge profiles for ultrathin 2D-MoO$_2$ electrodes at current density of 100 mA g^{-1}. (B) Rate capability of ultrathin 2D-MoO$_2$ anodes. (C) Cycle performances at current rate of 100 and 1000 mA g^{-1}. (D) Quantitative analysis shows the contribution of diffusion-controlled charge storage as a function of potential. (E) Ex situ high-resolution XPS spectra of the Mo 3d region in pristine (OCV), fully lithiated (0.005 V) and delithiated (3 V) ultrathin 2D-MoO$_2$ electrodes. (F) Ex situ high-resolution XPS spectra of the Li 1s region in lithiated (0.005 V) and delithiated (3 V) ultrathin 2D-MoO$_2$ anodes.

process times (referred to as 6 to 30 h). We noticed that the ex situ XRD can detect three principal phases, namely orthorhombic MoO$_3$, orthorhombic MoO$_{2.5}$(OH)$_{0.5}$, and monoclinic MoO$_2$ (see their crystal structures in Figure 3C−E). Early in the process (6 h), a part of layered MoO$_3$ was protonated and then converted to layered MoO$_{2.5}$(OH)$_{0.5}$. When increasing the reaction time to 12 h, the pure MoO$_{2.5}$(OH)$_{0.5}$ phase was observed, implying the full consumption of layered MoO$_3$. H$_2$O was then gradually eliminated from the MoO$_{2.5}$(OH)$_{0.5}$ interlayers with a prolonged reaction time. Simultaneously, the MoO$_{2.5}$(OH)$_{0.5}$ layers became closer and the reconstruction of Mo−O octahedra led to the formation of monoclinic MoO$_2$. The formation of the intermediate phase between MoO$_3$ and MoO$_2$ (MoO$_3$ → MoO$_{2.5}$(OH)$_{0.5}$ → MoO$_2$) during hydrothermal reaction suggests that pyrrole-induced evolution of MoO$_3$ does not follow the "direct reduction model" (eq 1) proposed for gaseous hydrogen reduction of MoO$_3$, wherein the diffusion of oxygen vacancies from the surface is believed to be the rate-determining step.[36] Our ex situ Raman studies (Figure 3B) further support this.
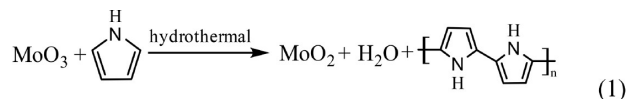
The slight blue shift of Raman peaks of MoO$_{2.5}$(OH)$_{0.5}$ (compared to MoO$_3$) again confirms that the protonation of MoO$_3$ under hydrothermal conditions leads to the topotactic formation of MoO$_{2.5}$(OH)$_{0.5}$ (Figure S7a), whereby only the Mo═O double bonds between the MoO$_3$ layers in [010] direction are reduced to Mo—O—H. We notably observed the existence of PPy (Raman peaks at 1371 and 1600 cm^{-1}) in the MoO$_3$-pyrrole homogeneous mixture (0 h, before hydro-

thermal reaction), suggesting that mixing the MoO$_3$ nanoribbons and pyrrole monomers together immediately triggers the polymerization of pyrrole. The corresponding TEM images (Figure S7b,c) confirm the above observation. On the basis of our experimental results, we propose the following mechanism (eqs 2−4) for the formation of MoO$_2$ nanoribbons, as schematically illustrated in Figure 3f: (1) Ultrathin PPy amorphous layer on MoO$_3$ surface was formed by MoO$_3$ "catalytic" polymerization when MoO$_3$ and pyrrole were mixed; the pyrrole simultaneously releases the H$^+$ ions (eq 2). (2) During hydrothermal treatment, the Mo═O double bonds in between the MoO$_3$ layers in [010] direction are reduced to Mo−O−H, resulting in the formation of intermediate phase MoO$_{2.5}$(OH)$_{0.5}$ (eq 3). In addition, the release of H$^+$ ions further promotes the polymerization and leads to thicker PPy layers. (3) With increasing time, H$_2$O is gradually eliminated from the intermediate MoO$_{2.5}$(OH)$_{0.5}$ phase, leading to a mild reconnection of the Mo−O octahedra and the subsequent formation of MoO$_2$ (eq 4). As these reactions are confined inside the PPy layers, the morphology and crystallinity of MoO$_2$ does not change significantly from the starting MoO$_3$ template. The reaction sequence can be summarized as follows

$$\text{MoO}_3 + \text{pyrrole} \xrightarrow{\text{hydrothermal}} \text{MoO}_2 + \text{H}_2\text{O} + \text{PPy} \quad (1)$$

$$\text{pyrrole} \xrightarrow{\text{MoO}_3} \text{PPy} + \text{H}^+ \quad (2)$$

$$\text{MoO}_3 + \text{H}_3\text{O}^+ \xrightarrow{\text{hydrothermal}} \text{MoO}_{2.5}(\text{OH})_{0.5} \quad (3)$$

$$\text{MoO}_{2.5}(\text{OH})_{0.5} \xrightarrow{\text{hydrothermal}} \text{MoO}_2 + \text{H}_2\text{O} + \text{O}_2 \quad (4)$$

Using this pyrrole-based reduction strategy, we have successfully prepared ultrathin 2D nanoribbons of normally nonlayered MoO_2 (2D-MoO_2) from exfoliated MoO_3 (1−3 atomic layers thick) nanoribbon templates. Figure 4A displays the digital photos of as-prepared and exfoliated MoO_3 nanoribbon dispersion and their corresponding thin films. The obvious color change implies the successful exfoliation of layered MoO_3 nanoribbons.[37] In fact, the dramatic decrease of XRD intensities of MoO_3 (0k0) planes proves the successful exfoliation of layered MoO_3 (Figure S8). As Figure 4B,C conveys, the exfoliated MoO_3 still exhibits a nanoribbon shape with a length of 1−2 μm. Atomic force microscopy (AFM) analysis reveals that these exfoliated MoO_3 nanoribbons are a few nanometers thick on average, corresponding to 1 to 3 atomic MoO_3 layers (Figure 4D,E and Figure S9). Since MoO_2 is topotactically converted from MoO_3, we believe that the as-obtained 2D-MoO_2 sheets are only 1−3 unit cells thick. Transmission electron microscopy, scanning TEM (STEM), and high-resolution TEM (HRTEM) images (Figure 4F−H) clearly reveal that the 2D-MoO_2 maintains well-defined core−shell configuration. The lattice plane distances in Figure 4H is 0.34 nm, which fits well to the (−111) interplanar spaces in monoclinic MoO_2. Our statistical analysis (Figure S10) shows that the PPy shell in 2D-MoO_2 is about 3−5 nm thick. Figure S11a exhibits the AFM image of the individual 2D-MoO_2 nanoribbon, confirming its ultrathin nature (∼6.7 nm). Considering the thickness of amorphous PPy shells, it is believed that the 2D-MoO_2 cores are approximately 1 nm thick, which corresponds to a few MoO_2 atomic planes. In stark contrast, the thickness of MoO_2/PPy obtained from non-laminated MoO_3 is around 100 nm (Figure S11b). Additionally, the XPS results of ultrathin 2D-MoO_2 (Figure S11c) further confirm the formation of high-quality MoO_2 after pyrrole monomer reduction. These ultrathin 2D-MoO_2 nanoribbons are composed of 65.3% MoO_2 and 34.7% PPy (Figure S11d), which is very close to that of unexfoliated-MoO_2/PPy (ue-MoO_2). Moreover, our detailed elemental distribution studies on the PPy-covered 2D-MoO_2 nanoribbons also verify their well-defined geometry and the uniform feature of PPy shells (Figure 4I,J). Therefore, we could conclude here that high-quality, ultrathin PPy-covered 2D-MoO_2 (∼1 nm thick MoO_2) nanoribbons have been achieved, which we have then tested as electrode materials for LIBs and microsupercapacitors.

We first evaluated the electrochemical performance of the ultrathin 2D-MoO_2 nanoribbons as LIB anodes. All working electrodes were fabricated using the vacuum filtration method (ultrathin 2D-MoO_2/CNT = 9:1; in wt %), resulting in binder-free electrodes. We recorded the deep galvanostatic charge−discharge (CD) profiles of ultrathin 2D-MoO_2 electrodes at the current density of 100 mA g^{-1} in the voltage range of 0.005−3.0 V. Note that our control experiments reveal that the capacity contribution from PPy is considerably limited (about 10−15 mAh g^{-1}; Figure S12). The CD curves (Figure 5A) for ultrathin 2D-MoO_2 show a first discharge/charge capacity of 3088/1875 mAh g^{-1} (based on the mass of MoO_2) with an initial Coulombic efficiency of ca. 61%. This irreversible capacity of the first CD scan is mainly due to the consumption of Li-ions during the SEI layer formation. We noticed that on the second and fifth cycles, the Coulombic efficiency of ultrathin 2D-MoO_2 anode increases up to >95% and then >99%, respectively. As Figure 5A shows, the ultrathin 2D-MoO_2 electrodes retain a high reversible capacity of 1528 mAh g^{-1} after 50 cycles. Furthermore, no pronounced charge/

discharge plateaus could be observed in the CD profiles. The sloped feature in the voltage profiles implies fast Li uptake and removal kinetics in the ultrathin 2D-MoO_2 electrodes. As an important performance indicator, the rate performance of these 2D electrodes was investigated. The good rate capability of 2D-MoO_2 is illustrated in Figure 5B, where the current density was increased stepwise from 0.1 to 10 A g^{-1} and returned to 0.1 A g^{-1}. The measured discharge capacities at 0.1, 0.5, 1, 5, and 10 A g^{-1} were 1752, 1268, 682, 434, and 198 mAh g^{-1}, respectively. Of note, the discharge capacity of these 2D-MoO_2 electrodes recovered to 1540 mAh g^{-1} when the current density was returned to 0.1 A g^{-1}, suggesting that the ultrathin 2D-MoO_2 anodes can tolerate high-rate cycling without anode degradation. As apparent in Figure 5C, these MoO_2 anodes offer a reversible capacity of 1516 mAh g^{-1} after 100 continuous CD cycles at the current rate of 100 mA g^{-1}. Impressively, even when the 2D-MoO_2|Li cell was cycled at a high current density of 1,000 mA g^{-1}, the ultrathin 2D-MoO_2 anodes still delivered a capacity of 489 mAh g^{-1} after 1,050 CD cycles, demonstrating their excellent cycling stability. To better understand their behavior, some ultrathin 2D-MoO_2-based cells were disassembled after 1,050 cycles at 1,000 mA g^{-1} and investigated by TEM. As may have been expected from the excellent cycling performance, the ultrathin 2D-MoO_2 anodes maintained their original morphology very well (Figure S13). In contrast with ultrathin 2D-MoO_2, we found that the MoO_2 formed from thick ue-MoO_3 nanoribbons (100 nm thick MoO_2/PPy) delivered ordinary Li storage capability (280 mAh g^{-1} at 100 mA g^{-1} after 20 cycles; Figure S14). In an attempt to understand the origin of the fast kinetics in ultrathin 2D-MoO_2 (MoO_2 ∼ 1 nm thick), we quantitatively separated the diffusion-controlled contribution and capacitive contribution to the measured current, according to Dunn et al.[38] Figure 5D presents the typical voltage profile for the diffusion-controlled current (red region) in comparison with the total current at the scan rate of 1 mV s^{-1}. An obvious capacitive contribution (48.2%) is obtained for the ultrathin 2D-MoO_2 electrode. Even as the scan rate decreased to 0.1 mV s^{-1} (Figure S15), the role of capacitive contribution is still apparent (∼23%). It is believed that such a huge capacitive contribution is due to the unique ultrathin 2D structure, which leads to a high surface-to-volume ratio and significantly shortens the Li-ion diffusion length in the 2D-MoO_2 anodes.

In Figure S16a, the cyclic voltammetry (CV) of this ultrathin 2D-MoO_2 electrode at 0.1 mV s^{-1} displays an obvious reduction peak at 1.13 V and a pronounced oxidation peak at 1.48 V, which correspond, respectively, to the insertion and extraction of Li into MoO_2 crystals (MoO_2 → Li_xMoO_2 → MoO_2). The CV and CD curves also indicate that most of the capacity of these ultrathin 2D-MoO_2 nanoribbons derives from the reaction below approximate 0.75 V. The intercalation process between 3 and 0.75 V shows a reversible intercalation capacity of about 400 mAh g^{-1} (Figure S16b), which is close to our DFT predicted value (493 mAh g^{-1}). This observation is consistent with our theoretical calculation showing that much higher intercalation capacity could be achieved in ultrathin 2D-MoO_2. It should be noted that the total reversible capacity of ultrathin 2D-MoO_2 is around 1500 mAh g^{-1} between 0.005 to 3.0 V, which is much higher than its theoretical value (840 mAh g^{-1}; assuming a four-electron redox reaction). Obviously, this immense difference suggests that the extraordinarily high reversible LIB capacity in the ultrathin 2D-MoO_2 samples is not based on the "intercalation/conversion" mechanism. We
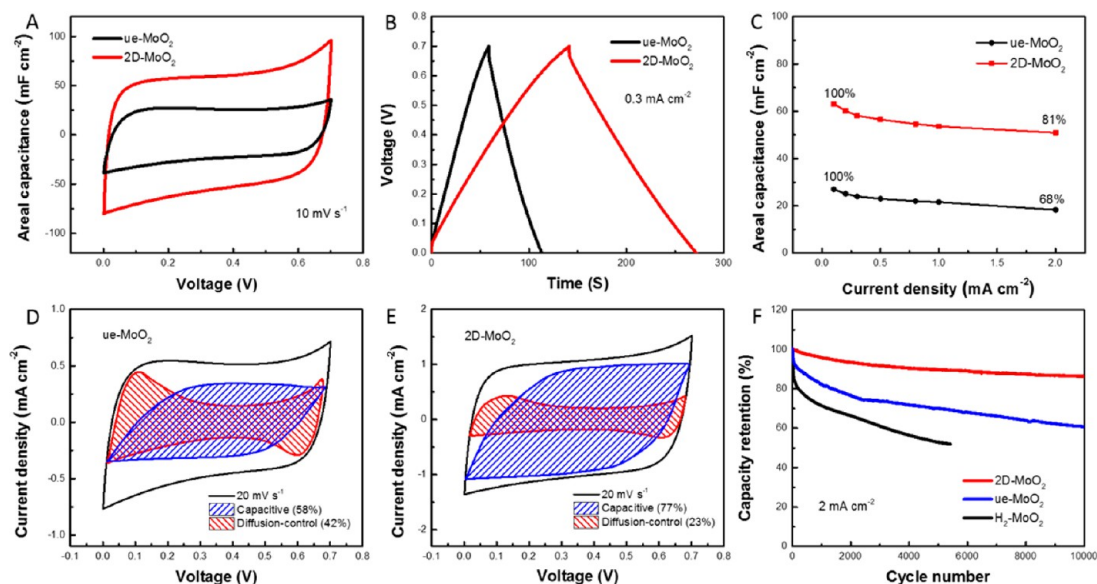
Figure 6. Electrochemical characteristics of the ultrathin 2D-MoO$_2$ nanoribbons corresponding to the MSC performance. (A) Voltammetric sweep at 10 mV s^{-1} for ue-MoO$_2$ and ultrathin 2D-MoO$_2$-based MSCs, and their corresponding (B) galvanostatic charge−discharge scan at 0.3 mA cm^{-2}. (C) Areal capacitance as a function of current density between 0.1 to 2 mA cm^{-2}. Quantitatively separate the diffusion-controlled capacity and capacitive capacity of (D) unexfoliated and (E) ultrathin 2D-MoO$_2$-based MSCs. These data indicate that the capacitive charge storage for ultrathin 2D-MoO$_2$ is much larger than its unexfoliated analogues. (F) Long-term cycling stability of different MoO$_2$-based MSCs.

believe that the ultrathin 2D geometry of MoO$_2$ enables electrochemical reactions that cannot occur in the thick or bulk MoO$_2$. One possible reaction is the formation of metallic Li around the Li$_x$MoO$_2$ crystals, which could markedly increase the measured capacity. To test this hypothesis, we carried out ex situ XPS and XRD studies. Figure 5E depicts the high-resolution XPS spectra of Mo 3d. The peak fitting analysis of pristine ultrathin 2D-MoO$_2$ (open circuit voltage; OCV) shows that its Mo 3d$_{5/2}$ peak is located at 231.7 eV. In fully lithiated samples or discharged state (0.005 V), we only observe one kind of Mo species where the Mo 3d$_{5/2}$ peak is located at 231 eV, which corresponds to the formation of Li-intercalated MoO$_2$ (Li$_x$MoO$_2$). We can also conclude that no free Mo metal exists after deep discharge (since Mo 3d$_{5/2}$ peak for Mo occurs at ∼227 eV).[39,40] Furthermore, the Mo 3d$_{5/2}$ peak of fully lithiated MoO$_2$ perfectly returns to 231.7 eV when it is charged to 3.0 V, demonstrating the excellent Li storage reversibility of ultrathin 2D-MoO$_2$. The Mo 3d$_{5/2}$ peak located at 230.1 eV in fully delithiated ultrathin 2D-MoO$_2$ may originate from oxygen-vacancy-rich MoO$_x$ that might be formed during the charging process. Interestingly, detailed analysis of Li 1s high-resolution XPS spectra of a fully lithiated electrode (Figure 5f) reveals four contributions at 56.4, 55.3, 54.8, and 54.2 eV, corresponding respectively to LiF,[41] Li$_2$CO$_3$,[42] Li$_x$MoO$_2$ and metallic Li.[43,44] The appearance of metallic Li component (Li 1s at 54.2 eV) strongly supports our hypothesis that the formation of the metallic Li phase is responsible for such a high capacity below approximate 0.75 V. Moreover, the reversible generation and consumption of metallic Li and Li$_x$MoO$_2$ during CD scans (from 3.0 to 0.005 V) is evident for stable Li storage in 2D-MoO$_2$. Figure S16c depicts ex situ XRD patterns of an ultrathin 2D-MoO$_2$ anode during the first CD cycle. Note that we cannot observe the MoO$_2$ diffraction peaks, probably due to its ultrathin nature. It is clear that there were no Mo nanocrystals formed when these anodes reached 0.005 V, suggesting that the conversion reaction did not take place. However, as evident in Figure S16d, we noticed the generation of Li$_2$O after 1 day of

exposure to air of the fully lithiated electrode. This newly formed Li$_2$O likely originates from the oxidation of amorphous metallic Li in fully lithiated MoO$_2$, which may be circumstantial evidence to prove the storage of Li as an amorphous-like, metallic phase in the ultrathin 2D-MoO$_2$. Thus, we believe that our ex situ XPS and XRD studies successfully demonstrate that these ultrathin 2D-MoO$_2$ anodes do not undergo a conversion reaction.[6]

Encouraged by the promising LIBs results, we evaluated the performance of symmetrical microsupercapacitors (MSCs) using these ultrathin 2D-MoO$_2$ nanoribbons as electrodes, with PVA/LiCl gel electrolyte. The CVs and CDs of the MoO$_2$ based quasi-solid-state microsupercapacitors are presented in Figure 6A,B. The CVs and CDs have, respectively, a rectangular and triangular shape typical of capacitive behavior. The areal capacitances versus current densities for the MSCs are calculated and included in Figure 6E. Significant performance differences are observed between the ultrathin 2D-MoO$_2$ and ue-MoO$_2$. The ultrathin 2D-MoO$_2$ MSC exhibits an areal capacitance of 63.1 mF cm^{-2} at 0.1 mA cm^{-2}, whereas that of ue-MoO$_2$ MSC is only 27 mF cm^{-2} at 0.1 mA cm^{-2}, suggesting about 2.4-folds increase of areal capacitance after thinning MoO$_2$ into 2D configuration. Moreover, ultrathin 2D-MoO$_2$ delivers better rate capability compared to its unexfoliated MoO$_2$ counterpart. They reached 50.9 mF cm^{-2} at 2 mA cm^{-2} with 81% retention. However, ue-MoO$_2$ retains only 68% of its initial areal capacitance at 2 mA cm^{-2}. We employed sweep voltammetry to provide greater insight into the difference in charge storage kinetics of 2D and ue-MoO$_2$ MSCs.[45] The data shown in Figure 6D,E indicate that capacitor-like charge storage in ultrathin 2D-MoO$_2$ occurs to a much greater extent compared to its unexfoliated analogue (77% versus 58%), implying faster kinetics for Li storage. This behavior further implies that these ultrathin 2D-MoO$_2$ materials are more favorable for high-rate energy storage applications. Further-more, we show that the areal capacitance of ultrathin 2D-MoO$_2$ MSC was stable over 10,000 cycles (86% retention; Figure 6F),

superior to ue-MoO$_2$ and H$_2$−MoO$_2$. Note that while PPy is highly inactive for capacitive Li-ion storage (Figure S17), it still helps to stabilize the electrodes and prevent the formation of an undesired surface amorphous coating on highly conductive MoO$_2$. These results evidence that ultrathin 2D-MoO$_2$ exhibits significantly enhanced MSC performance, including higher capacity, better rate capability, and longer lifespan, when compared with ue-MoO$_2$, which can be attributed to its unique 2D geometry. Figure S18 presents a volume-normalized Ragone plot. In comparison with other state-of-the-art systems, our devices offer the best performance in terms of volumetric energy and power density in the parallel-plate configuration. Specifically, ultrathin 2D-MoO$_2$ MSC offer a volumetric energy density of 17.2 mWh cm^{-3} at the power density of 0.35 W cm^{-3}. Impressively, with the increase of power density from 0.35 to 8.7 W cm^{-3}, the energy densities drop very slowly from 17.2 to 13.8 mWh cm^{-3}. Getting a high power density without a large sacrifice of energy density further indicates that the ultrathin 2D-MoO$_2$ is indeed promising for capacitive Li-ion storage. To further visually illustrate the potential of our ultrathin 2D-MoO$_2$ microsupercapacitor for practical application, we show that our prototype device (three cells in series) can power a red LED (Figure S19).

In summary, we report anomalous Li storage capacity in atomically thin 2D sheets of nonlayered MoO$_2$. These unique electrodes performed exceptionally well in both Li-ion batteries and microsupercapacitors. A novel monomer-assisted reduction process was developed to produce high-quality 2D sheets of nonlayered MoO$_2$. We demonstrate that our topotactical synthesis process introduces a general strategy that can be used to produce 2D nanostructures of other nonlayered oxides and sulfides. When used as LIB anodes, these ultrathin 2D-MoO$_2$ electrodes demonstrate an extraordinary reversible capacity as high as 1516 mAh g^{-1} after 100 cycles at the current rate of 100 mA g^{-1} and 489 mAh g^{-1} after 1050 cycles at 1000 mA g^{-1}. Our ex situ XPS and XRD studies reveal a Li-storage mechanism consisting of an intercalation reaction and the formation metallic Li phase in these 2D electrodes. In addition, the 2D-MoO$_2$-based microsupercapacitors exhibit a high areal capacitance (63.1 mF cm^{-2} at 0.1 mA cm^{-2}), good rate performance (81% retention from 0.1 to 2 mA cm^{-2}), and superior cycle stability (86% retention after 10,000 cycles). Furthermore, ultrathin 2D-MoO$_2$ MSCs offer a volumetric energy density of 17.2 mWh cm^{-3} at the power density of 0.35 W cm^{-3}. With the increase in power density from 0.35 to 8.7 W cm^{-3}, the energy densities drop very slowly from 17.2 to 13.8 mWh cm^{-3}. Our work identifies a new pathway to make 2D nanostructures from nonlayered compounds, which results in drastically enhanced energy storage capability.

ASSOCIATED CONTENT

Ⓢ Supporting Information

The Supporting Information is available free of charge on the ACS Publications website at DOI: 10.1021/acs.nanolett.7b05298.

Experimental methods, details of the AIMD, and theoretical capacity calculation; supporting discussion and supporting characterization (PDF)

AUTHOR INFORMATION

Corresponding Author
*E-mail: husam.alshareef@kaust.edu.sa.

ORCID
Zhiguo Wang: 0000-0002-5652-5362
Xixiang Zhang: 0000-0002-3478-6414
Husam N. Alshareef: 0000-0001-5029-2142

Notes
The authors declare no competing financial interest.

REFERENCES
(1) Dunn, B.; Kamath, H.; Tarascon, J.-M. *Science* **2011**, *334* (6058), 928−935.
(2) Armand, M.; Tarascon, J.-M. *Nature* **2008**, *451* (7179), 652−657.
(3) Jiang, J.; Li, Y.; Liu, J.; Huang, X.; Yuan, C.; Lou, X. W. D. *Adv. Mater.* **2012**, *24* (38), 5166−5180.
(4) Grimaud, A. *Nat. Energy* **2017**, *2*, 17003.
(5) Gupta, S. *Nature* **2015**, *526* (7575), S90−S91.
(6) Shon, J. K.; Lee, H. S.; Park, G. O.; Yoon, J.; Park, E.; Park, G. S.; Kong, S. S.; Jin, M.; Choi, J.-M.; Chang, H.; Doo, S.; Kim, J. M.; Yoon, W.-S; Pak, C.; Kim, H.; Stucky, G. D. *Nat. Commun.* **2016**, *7*, 11049.
(7) Kim, H.-S.; Cook, J. B.; Tolbert, S. H.; Dunn, B. *J. Electrochem. Soc.* **2015**, *162* (5), A5083−A5090.
(8) Yang, L.; Gao, Q.; Tang, Y.; Wu, Y.; Holze, R. *J. Power Sources* **2008**, *179* (1), 357−360.
(9) Shi, Y.; Guo, B.; Corr, S. A.; Shi, Q.; Hu, Y.-S.; Heier, K. R.; Chen, L.; Seshadri, R.; Stucky, G. D. *Nano Lett.* **2009**, *9* (12), 4215−4220.
(10) Li, Y.; Tang, F.; Wang, R.; Wang, C.; Liu, J. *ACS Appl. Mater. Interfaces* **2016**, *8* (44), 30232−30238.
(11) Guo, B.; Fang, X.; Li, B.; Shi, Y.; Ouyang, C.; Hu, Y.-S.; Wang, Z.; Stucky, G. D.; Chen, L. *Chem. Mater.* **2012**, *24* (3), 457−463.
(12) Dahn, J.; McKinnon, W. *Solid State Ionics* **1987**, *23* (1−2), 1−7.
(13) Ku, J. H.; Jung, Y. S.; Lee, K. T.; Kim, C. H.; Oh, S. M. *J. Electrochem. Soc.* **2009**, *156* (8), A688−A693.
(14) Novoselov, K. S.; Geim, A. K.; Morozov, S. V.; Jiang, D.; Zhang, Y.; Dubonos, S. V.; Grigorieva, I. V.; Firsov, A. A. *Science* **2004**, *306* (5696), 666−669.
(15) Tan, C.; Zhang, H. *Nat. Commun.* **2015**, *6*, 7873.
(16) Du, G.; Guo, Z.; Wang, S.; Zeng, R.; Chen, Z.; Liu, H. *Chem. Commun.* **2010**, *46* (7), 1106−1108.
(17) Tsai, M.-L.; Su, S.-H.; Chang, J.-K.; Tsai, D.-S.; Chen, C.-H.; Wu, C.-I.; Li, L.-J.; Chen, L.-J.; He, J.-H. *ACS Nano* **2014**, *8* (8), 8317−8322.
(18) Chang, K.; Geng, D.; Li, X.; Yang, J.; Tang, Y.; Cai, M.; Li, R.; Sun, X. *Adv. Energy Mater.* **2013**, *3* (7), 839−844.
(19) Jing, Y.; Zhou, Z.; Cabrera, C. R.; Chen, Z. *J. Phys. Chem. C* **2013**, *117* (48), 25409−25413.
(20) Yang, D.; Lu, Z.; Rui, X.; Huang, X.; Li, H.; Zhu, J.; Zhang, W.; Lam, Y. M.; Hng, H. H.; Zhang, H. *Angew. Chem., Int. Ed.* **2014**, *53* (35), 9352−9355.
(21) Zheng, Y.; Zhou, T.; Zhao, X.; Pang, W. K.; Gao, H.; Li, S.; Zhou, Z.; Liu, H.; Guo, Z. *Adv. Mater.* **2017**, *29*, 1700396.
(22) Pour, N.; Gofer, Y.; Major, D. T.; Aurbach, D. *J. Am. Chem. Soc.* **2011**, *133* (16), 6270−6278.
(23) Larsson, P.; Ahuja, R.; Nytén, A.; Thomas, J. O. *Electrochem. Commun.* **2006**, *8* (5), 797−800.
(24) Yang, L.-M.; Bačić, V.; Popov, I. A.; Boldyrev, A. I.; Heine, T.; Frauenheim, T.; Ganz, E. *J. Am. Chem. Soc.* **2015**, *137* (7), 2757−2762.
(25) Li, X.; Dai, Y.; Li, M.; Wei, W.; Huang, B. *J. Mater. Chem. A* **2015**, *3* (47), 24055−24063.
(26) Cahangirov, S.; Topsakal, M.; Aktürk, E.; Şahin, H.; Ciraci, S. *Phys. Rev. Lett.* **2009**, *102* (23), 236804.

(27) Uthaisar, C.; Barone, V. *Nano Lett.* **2010**, *10* (8), 2838−2842.

(28) Tritsaris, G. A.; Kaxiras, E.; Meng, S.; Wang, E. *Nano Lett.* **2013**, *13* (5), 2258−2263.

(29) Jin, Y.; Shen, P. K. *J. Mater. Chem. A* **2015**, *3* (40), 20080−20085.

(30) Li, M.; Wei, Z.; Jiang, L. *J. Mater. Chem.* **2008**, *18* (19), 2276−2280.

(31) Sun, Y.; Hu, X.; Jimmy, C. Y.; Li, Q.; Luo, W.; Yuan, L.; Zhang, W.; Huang, Y. *Energy Environ. Sci.* **2011**, *4* (8), 2870−2877.

(32) Luo, W.; Hu, X.; Sun, Y.; Huang, Y. *J. Mater. Chem.* **2012**, *22* (11), 4910−4915.

(33) Li, T.; Beidaghi, M.; Xiao, X.; Huang, L.; Hu, Z.; Sun, W.; Chen, X.; Gogotsi, Y.; Zhou, J. *Nano Energy* **2016**, *26*, 100−107.

(34) Guo, C.-h.; Zhang, G.-j.; Shen, Z.-r.; Sun, P.-c.; Yuan, Z.-y.; Jin, Q.-h.; Li, B.-h.; Ding, D.-t.; Chen, T.-h. *Chin. J. Chem. Phys.* **2006**, *19* (6), 543.

(35) Hu, B.; Mai, L.; Chen, W.; Yang, F. *ACS Nano* **2009**, *3* (2), 478−482.

(36) Kennedy, M.; Bevan, S. *J. Less-Common Met.* **1974**, *36* (1−2), 23−30.

(37) Hanlon, D.; Backes, C.; Higgins, T. M.; Hughes, M.; O'Neill, A.; King, P.; McEvoy, N.; Duesberg, G. S.; Mendoza Sanchez, B.; Pettersson, H.; et al. *Chem. Mater.* **2014**, *26* (4), 1751−1763.

(38) Wang, J.; Polleux, J.; Lim, J.; Dunn, B. *J. Phys. Chem. C* **2007**, *111* (40), 14925−14931.

(39) Yao, H.; Baird, R.; Gandhi, H. *J. Catal.* **1983**, *84* (1), 8−14.

(40) Swartz, W.; Hercules, D. M. *Anal. Chem.* **1971**, *43* (13), 1774−1779.

(41) Zhang, T.; He, Y.; Wang, F.; Li, H.; Duan, C.; Wu, C. *Sep. Purif. Technol.* **2014**, *138*, 21−27.

(42) Fan, L.; Zhuang, H.; Gao, L.; Lu, Y.; Archer, L. *J. Mater. Chem. A* **2017**, *5*, 3483−3492.

(43) Contour, J.; Salesse, A.; Froment, M.; Garreau, M.; Thevenin, J.; Warin, D. *Journal de Microscopie et de Spectroscopie Electroniques* **1979**, *4* (4), 483−491.

(44) Grehk, T.; Johansson, L.; Gray, S.; Johansson, M.; Flodström, A. *Phys. Rev. B: Condens. Matter Mater. Phys.* **1995**, *52* (23), 16593.

(45) Kim, H.-S.; Cook, J. B.; Lin, H.; Ko, J. S.; Tolbert, S. H.; Ozolins, V.; Dunn, B. *Nat. Mater.* **2017**, *16*, 454−460.